An inclusive view of Saharan dust advections to Italy and the Central Mediterranean

G.P. Gobbi[a,*], F. Barnaba[a], L. Di Liberto[a], A. Bolignano[b], F. Lucarelli[c], S. Nava[c], C. Perrino[d], A. Pietrodangelo[d], S. Basart[e], F. Costabile[a], D. Dionisi[a], U. Rizza[f], S. Canepari[g], R. Sozzi[b], M. Morelli[b], M. Manigrasso[h], F. Drewnick[i], C. Struckmeier[i], K. Poenitz[j], H. Wille[j]

[a] Institute of Atmospheric Sciences and Climate, National Research Council, ISAC-CNR, 00133, Rome, Italy
[b] Latium Agency for Environmental Protection, ARPA-Lazio, 02100, Rieti, Italy
[c] Department of Physics and Astronomy, University of Florence, and I.N.F.N., 50019, Sesto Fiorentino, Italy
[d] Institute for Atmospheric Pollution Research, CNR, 00015, Monterotondo Stazione, Rome, Italy
[e] Earth Sciences Department, Barcelona Supercomputing Centre, BSC, 08034, Barcelona, Spain
[f] Institute of Atmospheric Sciences and Climate, National Research Council, ISAC-CNR, 00133, Lecce, Italy
[g] Department of Chemistry, University "Sapienza", 00185, Rome, Italy
[h] Department for Technological Innovation, DIT, INAIL, 00187, Rome, Italy
[i] Particle Chemistry Department, Max Planck Institute for Chemistry, 55128, Mainz, Germany
[j] Jenoptik ESW, now at Lufft GmbH, 70736, Fellbach, Germany

ARTICLE INFO

ABSTRACT

We address observations of physical and chemical properties of Saharan dust advections (SDA) as observed in the Central Mediterranean basin, within the framework of the LIFE + 10, DIAPASON project (www.diapason-life.eu). DIAPASON aimed at the definition of best practices and tools to detect and evaluate the contribution of Saharan dust to ground particulate matter (PM) loads. Polarization-sensitive, automated lidar-ceilometers (PLC) are one of the tools prototyped and used in the Rome area to reach this goal. The results presented in this study focus on: 1) the effectiveness of various observational tools at detecting and characterizing atmospheric dust plumes, and 2) processes and properties of Saharan dust advections reaching the central Mediterranean region. In this respect, the combination of numerical model forecasts and time-resolved (at least hourly) PLC or chemical observations was found to constitute an efficient way to predict and confirm the presence of Saharan dust. In the period 2011–2014, Saharan dust advections were observed to reach over Rome on about 32% of the days. In some 70% of these days the dust reached the ground in dry conditions, while 30% of advection days involved wet deposition. Dry (wet) deposition was found to maximize (minimize) in summer. The northern Sahara between Algeria and Tunisia (Grand Erg Oriental), was confirmed as the most frequent region of origin of the dust mobilized towards central Italy. Secondary source regions include northern Morocco and Libya. On a statistical basis, Saharan advections to Rome were preceded by increasing atmospheric pressure and stability. These conditions were found to favor the accumulation of aerosols related to local emission sources before the SDA reached the ground. Meteorology (precipitation and turbulence *in primis*) resulted to be an important modulator of PM concentrations during SDAs. Magnitude and timing of these factors should be well considered to correctly evaluate the dust share in PM loads or the related health effects. Saharan advections observed during DIAPASON affected particle concentrations down to diameters of about 0.6–1 μm, with number concentrations peaking at the 2.5 μm diameter range. These advections were associated with a significant increase in Si-rich particles containing a non-negligible fraction of water. Rainfall was observed to preferentially remove dust particles larger than 2 μm, causing a significant depletion in the Ca-rich fraction with respect to the Si-rich one. The increase in PLC depolarization ratios above 5%, as well as the hourly PIXE records of the Si/Ca ratio increasing above 1 were found to represent good markers for the actual presence of Saharan dust particulate matter, when Saharan advection conditions are occurring.

---

* Corresponding author.
  E-mail address: g.gobbi@isac.cnr.it (G.P. Gobbi).

1. Introduction

Advection of mineral dust from arid regions is one of the main sources of natural aerosols on Earth (Prospero et al., 2002; Ginoux et al., 2012; Knippertz and Stuut, 2014). The Sahara region is the most important source of mineral dust advections to southern Europe (e.g., Guerzoni et al., 1997; Goudie and Middleton, 2001; Evan et al., 2016). Saharan dust advections (SDA) to Mediterranean countries are modulated by meteorology along rather regular seasonal patterns (e.g., Barnaba and Gobbi, 2004; Knippertz and Todd, 2012; Gkikas et al., 2012; Pey et al., 2013). Typically, SDAs to the central Mediterranean occur during cyclonic conditions in winter, spring and fall and during anti-cyclonic conditions in summer (e.g., Gaetani et al., 2012). As a consequence, deposition of Saharan dust to the central Mediterranean is mostly dry in summertime and mixed (wet and/or dry) in the remaining months (e.g., Guerzoni et al., 1997). Extreme dust transport events are also frequent (e.g. Gkikas et al., 2016), and single outbreaks can account for more than 50% of the total annual Saharan dust deposition (Guerzoni et al., 1997). The northern Sahara region between 30°N and 35°N, extending in longitude from the Southern slopes of the Moroccan Atlas range to the Tunisian Erg Oriental (10°W-10°E), includes the principal sources of the mineral dust reaching the central Mediterranean (e.g., Prospero et al., 2002; Ginoux et al., 2012; Evan et al., 2016).

In terms of impact on air quality (AQ), Saharan advections to Southern Europe can result in important increases in the PM_{10} loads measured at the ground (e.g., Gobbi et al., 2007; Querol et al., 2009; Nava et al., 2012; Pey et al., 2013; Gobbi et al., 2013; Barnaba et al., 2017). These episodes can cause exceedances in both the daily and yearly PM_{10} limits set by the EU Air Quality Directive (2008/50/EC), i.e., $50\,\mu g/m^3$ for the daily average, and $40\,\mu g/m^3$ for the yearly average. When assessing PM_{10} exceedances, the European air quality legislation allows for subtracting the Saharan, as well as other natural contributions from the total PM_{10} loads observed at AQ stations. To determine SDA conditions, the specific EC Guidelines provided to implement Directive 2008/50 (EC, 2011) do not require direct evidence of the presence of dust. Such demonstration is delegated to a series of indirect information as satellite retrievals, model forecasts, and back-trajectory analysis.

Currently, Saharan dust advections are rather well predicted by a variety of numerical models (e.g., Kallos et al., 1997, 2007; Alpert et al., 2002; Grell et al., 2005; Kishcha et al., 2007; Basart et al., 2012; Georgoulias et al., 2018) and, in the absence of clouds, their horizontal extent can be observed by satellites (e.g., Kaufman et al., 2002; Tafuro et al., 2006; Breon et al., 2011; Ashpole and Washington, 2012). These methods have been widely used to characterize SDAs over the Mediterranean both in extent and optical depth (e.g., Barnaba and Gobbi, 2004; Antoine and Nobileau, 2006; Gkikas et al., 2013). Still, assessing how many of these dust overpasses reach the ground, and evaluating their share in PM_{10} mass is not a straightforward exercise. Even the most direct techniques (chemical analysis of collected dust) can be made uncertain by local mineral contaminants. On the other hand, a spatially extended, operational evaluation of such contributions is necessary to assess SDA's effects, in particular to implement the 2008/50/EC Directive.

The DIAPASON project (www.diapason-life.eu) was implemented to make the EC Guidelines simpler and sound at proving the presence and quantifying the share of Saharan dust at AQ monitoring stations. To reach this goal, DIAPASON proposed two new tools: i) a modified methodological approach, tailored to facilitate and extend the operational use of the EC-Guidelines by AQ agencies (this work is presented in Barnaba et al., 2017), and ii) prototypes of new remote-sensing devices, suitable for being integrated in AQ monitoring stations to attest the presence of mineral dust advections. These instruments are upgrades of the automated lidar-ceilometers (ALC), i.e., active remote-sensing devices capable of a continuous, affordable monitoring of PM vertical profiles in the whole troposphere (e.g., Haeffelin et al., 2011).

Standard ALC are currently commercialized and employed in EU countries and worldwide (e.g., the EUMETNET- E-Profile initiative (http://eumetnet.eu/activities/observations-programme/current-activities/e-profile/alc-network), the German Weather Service (DWD; https://www.dwd.de/EN/research/projects/ceilomap), and the Italian Alice-net (www.alice-net.eu), e.g., Dionisi et al., 2018; Diéemoz et al., 2018). In fact, these ALC systems cannot discriminate amongst aerosol types as polarization-sensitive lidars allow to do (e.g., Sassen, 1991). In this respect, the polarization lidar technique was demonstrated to be very effective at detecting SDAs both at single stations (e.g., Gobbi et al., 2000; Gobbi et al., 2003; Tafuro et al., 2006), and (mostly within the EARLINET project) at the European scale, (e.g., Ansmann et al., 2003; Papayannis et al., 2008). To this end, DIAPASON took in charge the development of prototypal polarization-sensitive lidar-ceilometers (PLC) to demonstrate their capability at assessing the presence of Saharan advections over the monitored region, along a year-round, 24/7 operational schedule, an almost impossible or over-expensive task for "standard" lidars. Such demonstration has been performed by deploying three PLC systems in the Rome region (central Italy), and running them over a one-year period since October 2013.

Within the DIAPASON project, two intensive campaigns provided the opportunity to collect detailed chemical and physical observations together with modelling of the Saharan dust advected to the central Mediterranean. A first exploitation of these observations allowed for setting up new recommendations to evaluate the SDA contribution to PM_{10} loads in Europe (Barnaba et al., 2017). To complete the description of DIAPASON's main outcomes, this paper will address: i) the general, long-term properties of SDAs as analyzed along the project (Section 3.1); ii) a detailed physical and chemical characterization of single SDAs (Section 3.2), and iii) an evaluation of the PLC prototype capability at certifying the presence of such advections in the operational manner required by AQ agencies (Section 3.2).

2. Methods

Hereafter we describe the observational set up and the modelling tools employed in the course of the project. A complementary description of these tools and relevant results can be found in Barnaba et al. (2017).

2.1. DIAPASON's target region

The pilot study area of DIAPASON was the Latium region in central Italy, in particular the Rome area (Fig. 1). To explore horizontal variability of dust advections, DIAPASON established three observational sites: 1) Downtown Rome (via Boncompagni); 2) Castel di Guido, a rural site some 30 km west of central Rome; and 3) Rome Tor Vergata, a semi-urban site some 20 km south-east of central Rome (Fig. 1b). Each station was equipped with a PLC. Full ARPA Lazio (Latium region environmental agency) AQ instrumentation was run at Castel di Guido and Rome Boncompagni. Conversely, Rome Tor Vergata home of the ISAC atmospheric supersite (CIRAS), hosted additional instrumentation for the characterization of aerosols (e.g., Section 2.3, and the Appendix Section). Observations aimed at providing a one-year characterization of SDA events occurring in the Rome area. During this year, two intensive observation periods (IOP1 and IOP2) were implemented, involving a variety of co-operative, detailed observations conducted in Tor Vergata (e.g., Struckmeier et al., 2016; Barnaba et al., 2017; Rizza et al., 2017).

2.2. The DIAPASON PLC prototype

As mentioned, lidars (light detection and ranging) systems are widely employed in the profiling of atmospheric aerosol properties (e.g., Weitkamp, 2005; Winker et al., 2009). Polarization-sensitive lidars allow for discriminating spherical (droplet-like) from non-
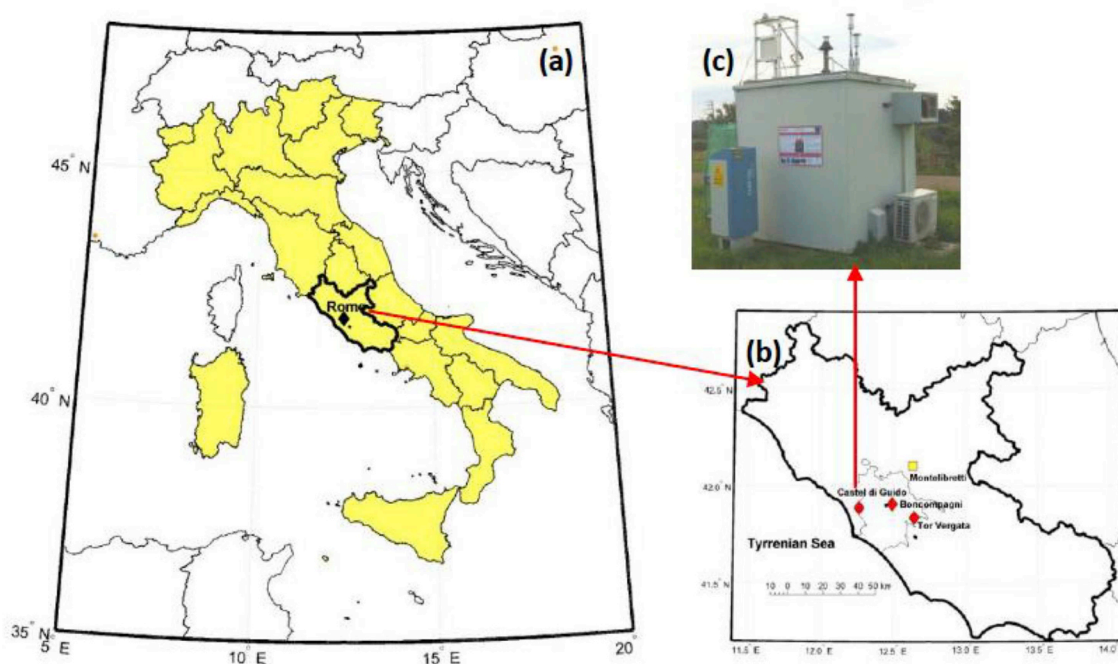
Fig. 1. a) map of Italy (yellow) with marked borders of the Latium region; (b) position of the DIAPASON monitoring sites (red diamonds) in the Rome area (light gray line) within the Latium region; c) image of the PLC and the Arpa Lazio air quality cabin at the Castel di Guido site.

spherical (e.g., dust, ice crystals) scatterers. This is made possible by the high depolarization the latter ones introduce in the backscatter signal with respect to the null depolarization of spherical scatterers (e.g., Sassen, 1991; Gobbi, 1998; Liu, 2009; Sakai et al., 2010).

Ceilometers are automatic, low-power lidars, originally developed to retrieve cloud-height by continuous sounding of the atmosphere. Latest generation of ceilometers proved to be capable of aerosol profiling (e.g., Wiegner and Geiβ, 2012; Diéemoz et al., 2018). By exploiting aerosol particles as a tracer, ceilometers also allow to infer the daily cycle of the mixing layer height (MLH), e.g., Eresmaa et al. (2006); Seibert et al. (2000); Haeffelin et al. (2011). So far, commercially available ceilometers have been single-channel instruments, i.e., unable to discriminate scatterers' shape. DIAPASON prototyped and tested the first polarization-sensitive ceilometer with the aim of creating an affordable, robust system to be widely used in the identification and profiling of dust-like aerosol layers. To this goal, the ceilometer manufacturer and project partner Jenoptik ESW (now Lufft) implemented the first PLC ever, as a development of their CHM15K - Nimbus system. As in the standard CHM15K, the PLC laser emits polarized pulses at 1064 nm, with a pulse rate of 5–7 kHz, and a pulse energy of 8 μJ. The receiver employs an avalanche photo-diode detector. In the PLC version, a second detector-chain is added to sense and store the cross-polarized atmospheric return. The two backscatter signals (parallel and cross-polarized) are calibrated by the half-wave plate method described in Mc Gill et al. (2002). Starting October 1, 2013 and until December 15, 2014 this PLC system has been operating at the DIAPASON site of Castel di Guido (Fig. 1) with the aim of demonstrating its 24/7 dust-layers detection and monitoring capabilities. At the same time, other polarization lidar systems were operated at the other two DIAPASON stations of Rome Boncompagni and Rome Tor Vergata (Fig. 1b). Thumbnails of these measurements were posted daily on the DIAPASON web-site (www.diapason-life.eu), and are also available at the ALICE-Net site (www.alice-net.eu).

As an example of PLC capabilities, Fig. 2 presents two days of the Jenoptik PLC measurements recorded in Rome on May 19 (Fig. 2a and

2b), and May 22 (Fig. 2c and 2d), 2014, along an important advection of Saharan dust which occurred during IOP2 (Barnaba et al., 2017; Rizza et al., 2017). Panels a) and c) detail each day's plot of PLC parallel backscatter range (R)-corrected signal (S_{par}), that is ln ($S_{par}*R^2$), up to 6 km altitude. Conversely, panels b), and d) illustrate the relevant volume depolarization ratio (δ_v%), that is the ratio between the inter-calibrated PLC's cross (S_{crs}), and parallel (S_{par}) backscatter signals. Therefore, δ_v% is a weighted average of the depolarization introduced in the lidar signal by the combined action of atmospheric aerosols and molecules (e.g., Gobbi, 1998). At the PLC wavelength (1064 nm), the ratio R between aerosol and molecular backscatter is R > > 1, typically 10–100. Therefore, the measured backscatter radiation is mostly generated by aerosol particles. As a consequence, the volume depolarization ratio (δ_v%) is a good-to-optimal approximation of the particulate matter depolarization (δ_P%), that is, the depolarization generated by aerosols alone. Since light backscattered by spherical particles keeps the original polarization plane, liquid droplets (e.g., rain or aerosols) are characterized by null or very low depolarization ratios. Conversely, non-spherical particles (e.g., ice crystals, mineral dust) can be discriminated by significantly larger depolarization ratios (e.g., Sakai et al., 2010). Dust–rich raindrops, as well as mixtures of liquid and dust aerosols depolarize as a function of their dust content. At 1064 nm, a typical depolarization ratio of pure Saharan dust away from its source is $\delta_P \approx 20\%$. Employing this value in Eq. 10 of Gobbi (1998) shows that depolarization values $\delta_v \approx \delta_P > 5\%$ (a safe level to avoid noise-induced errors) can be reached only when the non-spherical aerosol backscatter is larger than half the spherical aerosol one. The same relationship approximately holds in terms of aerosol volume (e.g., Dionisi et al., 2018). Therefore, in our PLC measurements mineral dust can be detected by a 5% depolarization threshold when its volume concentration is larger than half the coexisting liquid aerosols one.

Considering that backscatter signal increases with size and concentration of scatterers, the polarization lidar technique allows for discriminating clouds (highest backscatter, low/high depolarization when liquid/frozen), fogs (high backscatter, low depolarization, low
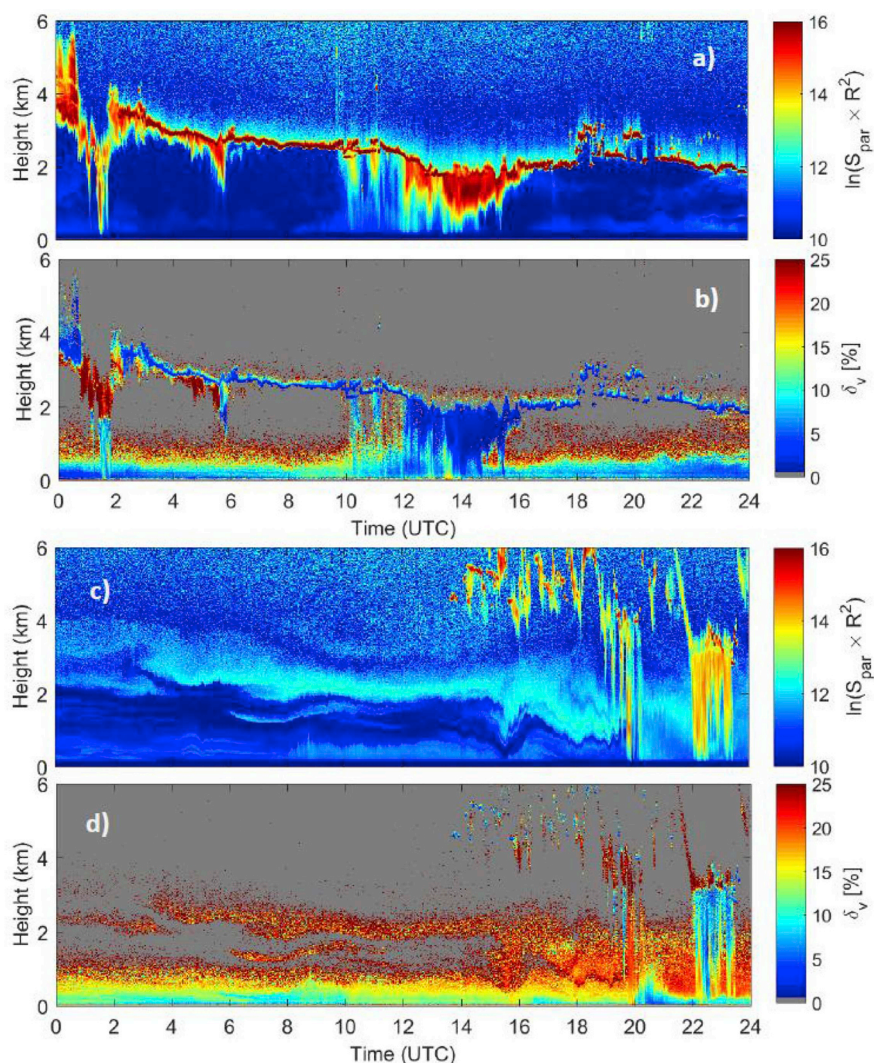
Fig. 2. Image plots of the Jenoptik PLC measurements recorded during an advection of Saharan dust observed in Rome on May 19 (panels a, b), and May 22 (panels c, d), 2014. Panels (a) and (c) depict PLC parallel backscatter, range-corrected signal (ln ($S*R^2$)) up to 6 km altitude. Conversely, panels (b) and (d) illustrate the relevant depolarization ratio (δ_v%).

altitude) and aerosol types (low backscatter and low/high depolarization in the case of liquid droplets/solid dust). Mineral dust plumes can be revealed by the coupled increase in backscatter and depolarization ratio they generate in the PLC signals (e.g., Gobbi et al., 2000). In the backscatter plots of Fig. 2 (panels a) and c)), clouds correspond to red colours, while aerosol signals range from pale blue to yellow. In the presence of thick clouds (as of May 19, panel (a)), the backscatter signal gets extinguished just above the initial layers. In this case the measurement characterizes only the lowermost portion of the cloud.

In Fig. 2a we can observe the lowermost part of a cloud-embedded dust layer (we know from model forecasts being originated in northern Africa) descending from about 4 to 2 km altitude, along the day of May 19, 2014. Precipitation appears as stripes dropping from cloud base towards the ground (but not always reaching it). Due to dominance of water droplets at backscattering the lidar pulses, the inner of the cloud shows very low depolarization (Fig. 2b). Conversely, clouds lowermost sectors and morning precipitation are characterized by higher depolarization ratios ($\approx$ 10–20%), distinctive of scavenging of desert dust by rain droplets. This is typical of dust-containing precipitation, where hundreds of micron-sized dust grains are embedded within millimetre-sized droplets (e.g., Appendix Figure D.2). Such dust scavenging is taking place up to about 12 UTC of May 19, 2014. In this period depolarization at the ground increases within the precipitation stripes

(Fig. 2-b). Conversely, the afternoon precipitation is characterized by very low depolarization, that is, this rain contains little or no dust at all. Furthermore, the strong precipitation removes most of the low-level dust layer (revealed by higher depolarization between ground and about 1.5 km altitude) thus temporarily cleansing the atmosphere down to the ground. When rain stops, the advection keeps bringing dust in the same atmospheric levels, i.e., up to about 1.5 km.

In the afternoon of May 22, 2014, Saharan dust layers descend towards the ground (Fig. 2d). A shallow ($\approx$ 500 m thick) mixing layer is noticed to develop between 8 and 15 UTC (Fig. 2c). Weak, depolarizing precipitation from the upper layer then occurs at about 20 UTC. Conversely, the stronger precipitation occurring at 22 UTC cancels for some time the 0–2 km, dust-generated depolarization signal. This period coincides with the peaking of the dust advection of IOP 2, which will be discussed in more detail in Section 3.2.1. These two illustrative days well summarize features of the dust advections that can be tracked and characterized by means of the analysis of PLC data.

2.3. DIAPASON observations and modelling

Starting October 1st, 2013, DIAPASON initiated a one-year monitoring phase aiming at the long-term characterization of Saharan dust advections to the Rome area. The two intensive observation periods

Table 1
Research groups and tools involved with the DIAPASON's measurement campaigns.

Group	Location	Measurement/Model type	Period	References
CNR-ISAC Institute of Atmospheric Sciences and Climate, Rome	Rome Tor Vergata Rome Boncompagni Castel di Guido	PLC, online aerosol optical properties	All Year	www.diapason-life.eu Barnaba et al. (2017) Appendix A
ARPA Lazio	Rome Tor Vergata Rome Boncompagni	PM_{10}-Meteo and turbulence	All Year	www.arpalazio.net/main/aria/sci/
Max Planck Institute for Chemistry, Mainz	Rome Tor Vergata	MoLa online aerosol characterization	IOP 1 & 2	Drewnick et al. (2012), Struckmeier et al. (2016)
INFN National Institute of Nuclear Physics, Florence	Rome Tor Vergata	1-h $PM_{2.5}$ & PM_{10} sampling for PIXE elemental analysis	IOP 1 & 2	Lucarelli et al. (2014) & 2018, Calzolai et al., (2015) Appendix B
CNR-IIA Institute for Atmospheric Pollution Research, Rome	Rome Montelibretti	24-h filters for chemical analysis; 48-h,10-stage impactor for SEM analysis	IOP 2	Perrino et al. (2016) Pietrodangelo et al. (2015) Appendix C & D
CNR-ISAC-Lecce	Lecce	WRF-Chem modeling	IOP 2	Rizza et al. (2017) Appendix E
Barcelona Supercomputing Centre	Barcelona	BSC-DREAM8b simulations	2011–2014	Basart et al. (2012), Appendix F

(IOP1 and IOP2) have been carried-out from October 22 to November 2, 2013, and between May 19 and May 27, 2014, respectively. These IOPs involved an extra number of observations and model simulations made in collaboration with networking research groups. The participating groups and references to relevant tools are summarized in Table 1. Supplemental description of the measurement techniques employed in the DIAPASON campaigns is provided in the Appendix Sections (A-F).

Results presented in the following sections include general properties of the Saharan dust advections determined on the basis of the DIAPASON one-year monitoring data (October 2013–September 2014), together with multi-year PM_{10} data from ARPA Lazio. BSC-DREAM8b model outputs (Basart et al., 2012) have been employed to reconstruct series of SDA timings and mass loads at Rome's ground level (e.g., Appendix F). Concurrently, detailed chemical and mineralogical dust properties have been determined during the IOPs to evaluate the quantitative properties of Saharan dust reaching the region, and to develop an improved methodology to evaluate the SDA contribution to PM loads (Barnaba et al., 2017). Finally, detailed model simulations by WRF-Chem (e.g., Grell et al., 2005) were performed to address the meteorological processes accompanying the generation and transport of the dust observed during the DIAPASON's second IOP (Rizza et al., 2017).

3. Results

Advections of Saharan dust affecting Italy and central Europe are mostly associated with North African depressions and cyclones, (e.g., Fiedler et al., 2014; Fiedler et al., 2015; Gaetani et al., 2012; Knippertz and Todd, 2012; Gkikas et al., 2012). The inter-annual variability of Saharan dust exports can be rather high over both the yearly (Guerzoni et al., 1997) and the decadal (Evan et al., 2016) timescales. Wet deposition, subsidence and boundary layer entrainment represent effective mechanisms to convey the dust to the ground. In terms of dust properties measured at the receptor point, processes occurring during the transit and deposition of the dust can lead to a variety of changes with respect to the original conditions. Hereafter we try characterizing these conditions by addressing separately both the long-term (year-scale) and short-term (event, i.e., IOP-scale) properties of the dust advections observed to reach central Italy during DIAPASON.

3.1. 'Long-term' properties of observed Saharan advections

The DIAPASON 'long-term' picture of Saharan dust advections is based on the one-year observations database (October 2013–September 2014), plus an additional analysis of BSC-DREAM8b simulations and HYSPLIT back-trajectories (Stein et al., 2015) addressing the 3-year period October 2011–September 2014, an extended time span chosen to support the statistics of this study.

3.1.1. The 3-year period: source regions and deposition

The density of transits in the planetary boundary layer (PBL) of the 5-day NOAA-HYSPLIT back-trajectories reaching Rome Boncompagni at 750 m MSL in the period October 2011–September 2014 is presented in Fig. 3. These were computed each day, starting at 6, 12 and 18 UTC, totalling about 1000 trajectories per year. The back-trajectories employed the GDAS meteorological data, and the 'vertical velocity' model.

Based on BSC-DREAM8b forecasts, back-trajectories were divided into 'Saharan dust-affected' and 'no-dust' cases (Fig. 3 left and right column, respectively). The back-trajectories were then analyzed to derive the spatial statistics of transits in the PBL they went through during their journey to Rome. A similar analysis, addressing the period 2001–2004, was presented in the supplemental material of Mallone et al. (2011), a study which evidenced some health consequences of SDAs observed in Rome. Similarly, most of the 2011–2014 Saharan advections analyzed in Fig. 3 originated north of 30°N, and the Grand Erg Oriental (at the southern slopes of the Atlas range at 33°N, between Algeria and Tunisia) is confirmed as the most frequent region of origin of the dust mobilized towards Italy (e.g., Prospero, 2003). Secondary source regions of the dust advected to Rome include northern Morocco and Libya. It is worth noticing that before reaching Rome most of these SDA trajectories travel in the Tyrrenian sea boundary layer. Conversely, PBL transits of non-SDA trajectories extend mostly to the NE (Slovenia and Austria) and NW (southern France), without intersecting northern
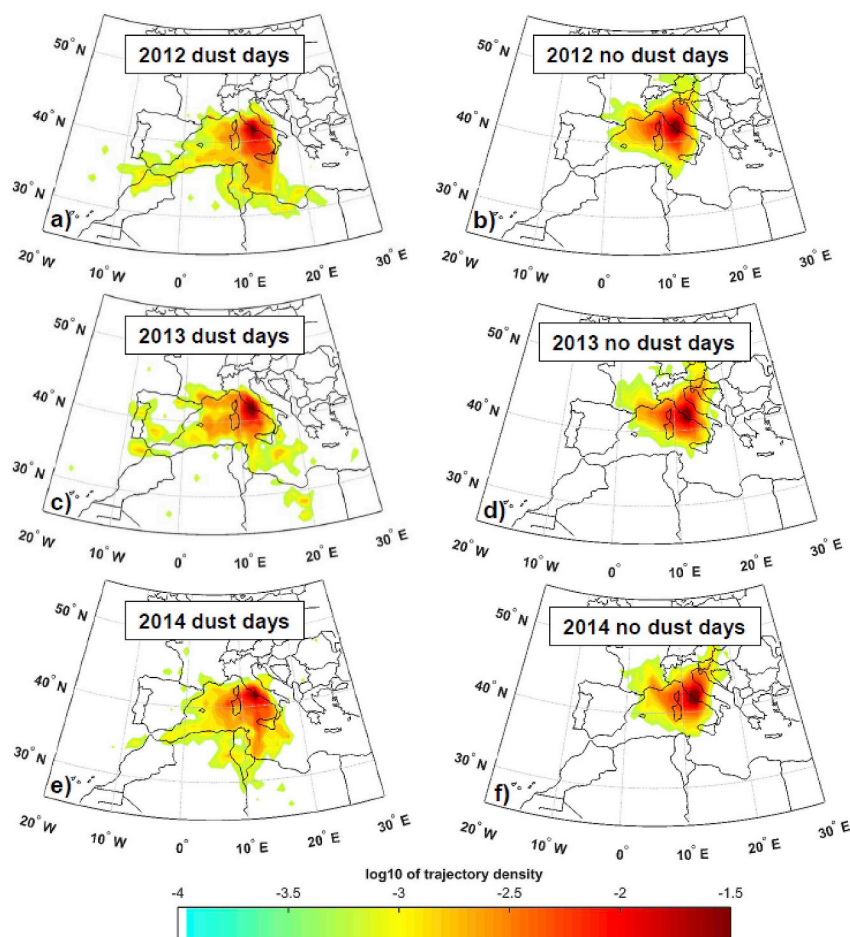
Fig. 3. Contour plots of the density of PBL transits of 5-day back-trajectories reaching Rome at 750 m MSL in the years 2012, 2013, and 2014, in the presence of SDA conditions (panels a, c and e, respectively) and in non-SDA days (panels b, d and f).

Africa (Fig. 3, right column).

Table 2 presents some statistics on the SDA properties studied within DIAPASON. In particular, the 3-year BSC-DREAM8b simulations pointed-out that in this period (October 2011–September 2014) some 32% of the days were affected by SDA transiting above Rome. About 30% of the advection's time involved wet deposition, while about 70% involved dry transport to the ground. Only 11% of wet deposition occurred in summer, while 33% of the total dry deposition times occurred in summertime. Also in Table 2, are reported the average ground-level PM$_{10}$ loads (for single advection days, and for the whole year) associated with the SDA events occurring in the period 2011–2014 (see also Barnaba et al., 2017).

In the DIAPASON one-year monitoring period described in the following section, the occurrence of dust overpasses and of ground-

deposition (validated by PLC observations) was 33% and 25% of the time, respectively. These numbers are in good agreement with the frequency of Saharan dust advections reported to reach Rome in the longer periods 2011–2014 (Table 2), and in 2001–2004 (Gobbi et al., 2004, 2013).

3.1.2. The 1-year period: meteorology and mixing layer's roles

Physical and meteorological variables of relevance to SDA, as recorded during the DIAPASON one-year observation time (October 2013–September 2014), are presented in Fig. 4. Days when BSC-DREAM8b forecasted the presence of Saharan dust at Rome's ground are marked by yellow squares. To better perceive the main drivers of Rome's PM loads during DIAPASON, Fig. 4 includes the records of daily-averaged turbulence kinetic energy (TKE, blue squares), daily

Table 2
Three-year (October 2011–September 2014) statistics of SDA properties observed in Rome.

| VARIABLE	Value	SOURCE
% of SDA days	32	BSC-DREAM8b
% days with SDA dust at ground	22	BSC-DREAM8b
% dry deposition time during SDAs.	70	BSC-DREAM8b
% wet deposition time during SDAs.	30	BSC-DREAM8b
Year average SDA impact on PM$_{10}$ (μg/m^3)	1.3 ± 0.3	Barnaba et al. (2017)
Average PM$_{10}$ increase in SDA-day (μg/m^3)	10.2 ± 1.3	Barnaba et al. (2017)
Min-Max number of PM$_{10}$ exceedances per year	41–57	Barnaba et al. (2017)
Min-Max number of SDA-induced PM$_{10}$ exceedances per year	4–13	Barnaba et al. (2017)
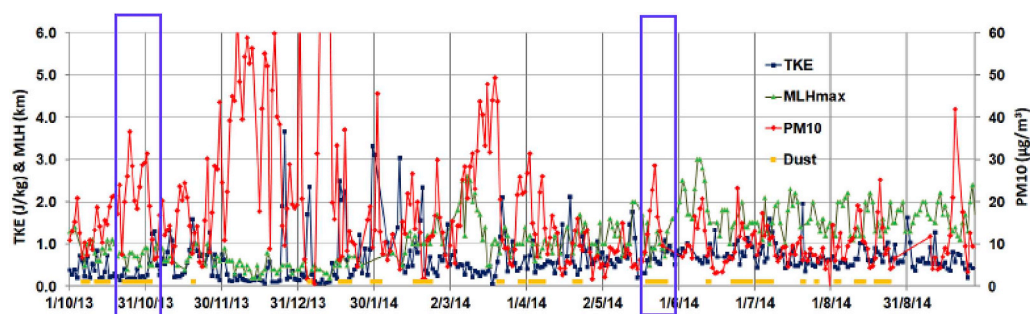
Fig. 4. One–year, daily records of TKE (blue squares, left axis), maximum MLH (green triangles, left axis), PM_{10} (red diamonds, right axis), and SDA flag (yellow squares when on) measured in Rome in the period October 1, 2013–September 30, 2014. The two purple boxes include the two DIAPASON's IOP periods. (For interpretation of the references to colour in this figure legend, the reader is referred to the Web version of this article.)

maximum mixing layer height (MLH, green triangles), and daily-averaged PM_{10} (red stars). TKE is the mean kinetic energy per unit mass, associated with atmospheric shear, friction or buoyancy. TKE is a good indicator of the atmospheric convective and wind-shear dispersion potential (e.g., Srivastava and Sarthi, 2002). It was retrieved from the Arpa Lazio sonic anemometer measurements performed at the Rome-Boncompagni site. In Rome, high TKE is associated with clean atmospheric conditions, often generated by northerly circulation.

The MLH characterizes the pollutants dilution capability of the lower troposphere. MLH is mainly associated with convection, that is, it has a sinusoidal behaviour, reaching maximum values in the middle of

the day and in summertime (e.g., Garratt, 1994). In this analysis the MLH was inferred by an operator-assisted analysis (e.g., Haeffelin et al., 2011; Angelini et al., 2014) of the lidar-ceilometer data recorded at Rome Boncompagni.

Together with atmospheric pressure and precipitation, TKE and MLH are the principal meteorological modulators of pollutant concentrations. The low-frequency patterns of both TKE and MLH in Fig. 4, show a summer maximum 2–3 times larger than the winter minimum for both variables. Conversely, the high frequency variability (daily) is mostly associated with TKE bursts occurring in wintertime. Purple boxes in Fig. 4 encompass the two DIAPASON's IOP periods, called on the basis of forecasts of significant Saharan dust advections. These periods are: i) October 22 - November 2, 2013 (maximum predicted PM_{10} dust mass of about $20\,\mu g/m^3$), and ii) 19–27 May, 2014 (maximum predicted dust mass in PM_{10} of about $80\,\mu g/m^3$). Actual measurements (reported in Barnaba et al., 2017) show the maximum increase in daily PM_{10} associated with these two SDAs. to be of 10, and $20\,\mu g/m^3$, respectively.

Typical values of meteorological variables associated with the SDAs which occurred during this one-year period are presented in Fig. 5. Here are plotted the median levels of the MLH, TKE, PM_{10}, and atmospheric pressure hourly data collected during the eighteen SDA events recorded in Rome along this year. The x-axis in Fig. 5 spans from 7 days before to 7 days after the dust 'touch-down' (set at time zero). Main outcomes of this analysis are the occurrence of systematic increases in pressure and PM_{10} load, coupled with a decrease in MLH, which precede the touch-down. Together with a flat behaviour of the TKE, these records indicate that stable conditions typically occurred before the arrival of dust. This condition results into a systematic increase in PM loads starting some 6 days ahead of the dust appearance at the ground (Fig. 5d). Such a pattern was also observed to occur over the broader area of Latium and Tuscany (Barnaba et al., 2017), and in previous years (Gobbi et al., 2013).

To correctly attribute PM loads to SDAs, it is then important to separate 'pre' from 'during'- advection times. Even though a general decrease in MLH (and flattening of the TKE) are visible during the days preceding the SDA event, we typically observed an increase in MLH to occur right at time zero, with an increase in TKE occurring during the following two days. On the whole, this indicates the dust touch-down to be usually associated with increasing turbulence, precipitation and, as expected, with dust-increased PM_{10} loads. In fact, the median rise in PM_{10} registered during the days just preceding the SDAs touch-down was comparable to the median increase associated with the dust events themselves (Fig. 5d), i.e., DIAPASON found SDAs meteorology (mostly high pressure conditions) to generate a non-dust, PM increase right before dust reaches the ground. The discussion in Section 3.2.5 will confirm this increase to affect PM_1 loads from local emission sources. In general, during the SDA events we observed the concentration of $0.56\,\mu m$ diameter particles to follow more closely the pattern of the atmospheric pressure than particles coarser than $0.8\,\mu m$ ones (e.g.,
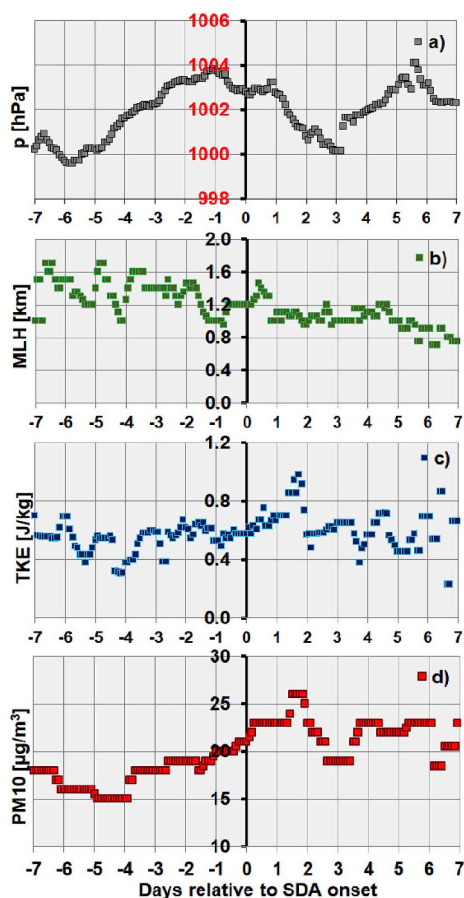

Fig. 5. Hourly data median values of: a) atmospheric pressure (hPa), b) mixing layer height (km), c) turbulence kinetic energy (J/kg), and d) PM_{10} ($\mu g/m^3$) during the 7 days preceding the SDA arrival at the ground (-7:0) and during the 18 SDA events (t > 0) which occurred during the DIAPASON one-year monitoring period.
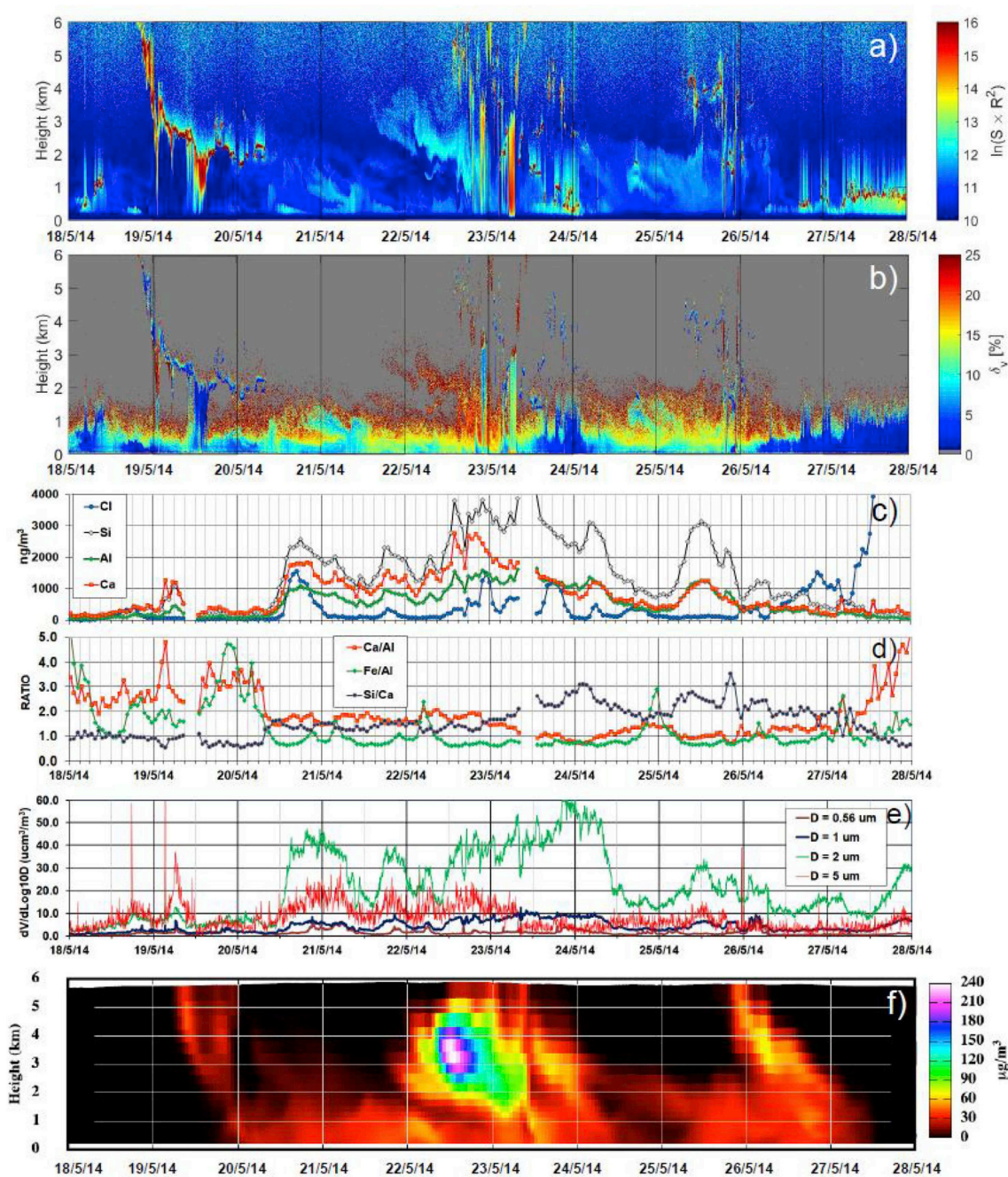
Fig. 6. Multivariable plot of the SDA event occurring from May 18 till May 27, 2014: Image plots of PLC range-corrected, parallel backscatter (a) and volume depolarization ratio (b) signals up to 6 km; (c) Cl, Si, Al and Ca concentrations in PM_{10} from PIXE analysis; (d) Ca/Al, Fe/Al and Si/Ca ratios of PM_{10} components from the PIXE analysis; (e) aerosol volume distribution (dV/dLogD) at aerodynamic diameters of 0.56, 1, 2 and 5 μm, as measured by the APS systems; (f) image plot of Saharan dust PM_{10} up to 6 km, as simulated by WRF-Chem.

discussion of Fig. 6 in Section 3.2.1). This latter dimensional class possibly represents a lower limit of the Saharan dust size distribution.

These results partly support the 'MLH-driven pollutant concentration effect' attributed to SDAs by Pandolfi et al. (2014), where SDA conditions in Barcelona were found to be statistically associated with significant decreases in MLH, therefore with a diminished atmospheric dilution capability. In our Rome record, such conditions pertain mainly to the days before the dust touch-down. Furthermore, pressure drop together with the increase in TKE and precipitation observed at the

ground during the SDA first days, indicate the possible occurrence of PM-reducing mechanisms along with the advent of the mineral dust. Such decreases in PM loads have been observed during some SDAs, especially in wintertime, when precipitation is more common. Overall, the increase in stability observed in Rome during the days preceding SDAs could also bear a role in the health effects associated with SDAs, e.g, Perez et al. (2008), Pandolfi et al. (2014), Stafoggia et al. (2016). In this respect, an exact timing of the pre and post dust intrusion phases appears to be important to separate the different mechanisms possibly

associated with them. It is worth noticing that Pandolfi et al. (2014) addressed the coastal site of Barcelona, where the yearly average MLH is of about 800 m, a fairly low value which suggests a dependence of the MLH on marine circulation (marine MLH is commonly lower than inland). Conversely, our records show the inland site of Rome to be characterized by a yearly average continental-type MLH of about 1200 m. Since in both cities SDA mainly approach from marine quadrants, it is likely that also the larger MLH reduction observed in Barcelona during SDAs is due to its proximity to the sea. All these mechanisms definitely need to be addressed in further specific studies based on multi-year analyses.

3.2. The single advection time-scale perspective from IOP2

In this section we address specific properties of single dust advections observed during DIAPASON. In particular, we focus on the May 2014 IOP2, since this was characterized by both a maximum number of measurements, and by detailed model simulations. Model forecasts and observations of Saharan dust advections are commonly used to trigger/validate each other. In DIAPASON we employed BSC-DREAM8b SDA forecasts to trigger observations (see also Barnaba et al., 2017), and WRF-Chem model runs to simulate mechanisms and physical properties of dust advections (Rizza et al., 2017).

3.2.1. Physical observations

Fig. 6 includes experimental data collected during the IOP2 at the DIAPASON sites of Castel di Guido (coastal), and Rome Tor Vergata (semi-urban, see Fig. 1). These data are plotted together with WRF-Chem, model calculations of dust PM_{10} loads for the period 18–27 May, 2014. In particular:

- panels (a) and (b): image plots of PLC range-corrected, parallel backscatter signal, and volume depolarization ratio (cross over parallel backscatter) up to 6 km altitude, respectively
- panel (c): time series of the Cl, Si, Al and Ca concentrations in PM_{10}, as retrieved by Particle-Induced X-ray Emission analysis (PIXE) of the collected filters (e.g., Sections 3.2.3, and Appendix B)
- panel (d): time series of the Ca/Al, Fe/Al and Si/Ca ratios of PM_{10} components, as retrieved by the analysis of the PIXE dataset
- panel (e): aerosol volume distribution (dV/dLogD) at aerodynamic diameters of 0.56, 1, 2 and 5 μm, as retrieved by the ISAC (18–20 May) and MoLa (20–27 May) aerodynamic particle sizer (APS) measurements (e.g., Appendix A)
- panel (f): contour plot of Saharan dust PM_{10} up to 6 km altitude, as simulated by WRF-Chem (Rizza et al., 2017).

As in Fig. 2, dust plumes in Fig. 6 can be identified by the concurrent increase in backscatter signals and depolarization ratios in the PLC measurements (panels (a) and (b), respectively). Conversely, spherical (liquid) aerosol particles generate an increase in backscatter signal alone. In this framework, the altitude position of the dust plumes is found to be well marked-out by depolarization ratios larger than 5%. Such values are typically encountered during SDAs. Still, it would be difficult to attribute such observations to a Saharan advection if it were not forecast by model and identified by PLC coincidence. Overall, the WRF-Chem simulations (Fig. 6f) well catch the timing and altitude distribution of the advection.

A combined interpretation of the PLC measurements (panels (a) and (b)) and of the WRF-Chem simulations (panel (f)), explains that the IOP2 advection was composed of four main pulses reaching aloft, over Rome, on 19, 21, 22 and 25 May, 2014, respectively (see also Rizza et al., 2017). Analysis of the history-making of these four plumes, and of their lidar imprints observed over Rome (e.g., Fig. 2 and 6) suggests they have formed and evolved in the following way:

- Plume 1: Generated by the union of several plumes: the first one originating in the afternoon of May 17 in the Grand Erg region comprised within 31–33°N, and 5-10°E), the second in the morning of May 18, 2014 at about 34°N-8°E (Algerian-Tunisian Southern Atlas, Grand Erg Oriental desert). Finally, a weaker third one, originating in the afternoon of May 18, 2014 at about 34°N-3°E (Algerian Southern Atlas, Grand Erg Occidental desert). All plumes were generated during local rainstorms, and then travelled towards Rome unaffected by significant precipitation. The combined plume reached Rome (at about 2.5 km above MSL) on May 19, undergoing some sporadic precipitation in the morning, and more intense precipitation in the afternoon. It then descended to the ground in the mid of May 20, 2014 (e.g., panels (a) and (b)).
- Plume 2: Originated without precipitation in the afternoon of May 20 at about 32°N-3°W (Southern Moroccan-Algerian Atlas). It travelled without important precipitation to reach above Rome (at 2–4 km above MSL) in the late afternoon of May 21. It then descended to the ground in the afternoon of May 22. Some intense precipitation from plume 3 superimposed to it in the evening (e.g., panels (a) and (b)).
- Plume 3: Had dry origin in the mid of May 21 at 33°N-2°E (Southern Algerian Atlas, Grand Erg Occidental), then travelled NE without significant precipitation. It reached high above Rome (3–7 km above MSL) in the afternoon of May 22, then rapidly descended to the ground along with precipitation events in the night between May 22 and 23 (e.g., panels (a) and (b)) and in the morning of May 23.
- Plume 4: Originated in dry conditions in the mid of May 24 at 34°N-3°E (Algerian Atlas southern slopes). It travelled within intermittent precipitation to reach above Rome (2–4 km above MSL) in the morning of May 25. Ground contact occurred in the mid of May 25, adding PM to the pre-existing dust load. The whole event was over on May 26 (e.g., panels (a) and (f)).

All these mineral dust plumes originated at the South of the Atlas Mountains, in northern Sahara regions rich in dry lakes (Chotts) and sand seas (e.g., Prospero et al., 2002; Ginoux et al., 2012; Dewitte et al., 2013; Journette et al., 2014).

Fig. 6 allows for reconstructing the temporal evolution of the most significant properties of this dust advection as observed in the Rome area: The dust plume reaches over Rome at about 4 km altitude in the morning of May 19 (Fig. 6a-b). Occasional, down-lift of dust particles is performed by light rain events (3 and 6 UTC), possibly evaporating before reaching the ground (e.g., Section 2.2). In the PLC traces this is evidenced by rain bands extending from the dust layer towards the ground (e.g., Fig. 6 a-b, and Fig. 2 a-b). Concurrently, values of Ca, Ca/Al and 5 μm sized particles strongly increase at the ground, suggesting rain is preferentially transporting down larger particles, rich in Calcium. Later on (10–15 UTC), precipitation starts much more intense, e.g., Fig. 6 a-b and Fig. 2 a-b. In this case, after an initial increase in 5 μm sized particles, dust wash-out (marked by the lowering depolarization) ends-up dominating with respect to near-ground subsidence. Conversely, when on May 20 at 9 UTC this dust plume reaches the ground, Ca/Al ratios decrease to 1.5, and the volume distribution is dominated by 2 μm particles, with 5 and 1 μm particles also increasing but not as much. These differing properties measured over samples of the same plume suggest that rather than differences in origins of the plume, wet-removal processes can play, at times, a leading role at determining the composition and size distribution of the Saharan dust reaching the ground. As in the latter case, the large-particles subsidence process was not observed during the following heavy rain events which occurred within the period May 22–23, 2014.

Ground deposition of the first plume is still going on at 12 UTC of May 22, when Plume 2 begins reaching the ground, mixing with plume 1 (e.g., Figs. 6 b and Fig. 2 c-d), with both Si/Ca and Ca/Al ratios

remaining in the range 1.5–2. Plume 2 starts dominating past 22 UTC. Correspondingly, the Si/Ca ratio starts increasing while Ca, Ca/Al, and 5 μm particle concentrations decrease, indicating the plume 2 as poorer in Ca and confirming Ca as typical for particles of the larger sizes. Along with some precipitation events, plume 3 mixes-in during the night with no major effects on components trends. Strong precipitation at 9 UTC of May 23 then removes most of the Ca-rich, 5 μm particles, while 2 μm ones and the Si/Ca ratio increase (the latter up to 3) during the following 24 h. As on May 19, precipitation affects mainly the larger, Ca-rich particles.

The effects of plumes 2 and 3 strongly decrease in the afternoon of May 24 (Fig. 6c). On May 25, plume 4 reaches the ground bringing a sharp increase in Si concentrations, and in 2, 5 and 1 μm particle's volume concentrations (Fig. 6, panels (c) and (e)). The effects of this last pulse almost vanish by the end of May 27th. As well as its beginning, the termination of the event is well marked by a low (< 5%) depolarization ratio at near-ground levels, low Si concentration, and low Si/Ca ratio. In fact, the Si/Ca ratio increasing above 1 appears to be a good marker of the dust presence along the whole event. In a comparable way, lidar depolarization ratios larger than 5% mark the increasing presence of non-spherical, dust particles.

Both total (i.e., PM_{10}) Si and Ca concentrations measured by PIXE grow during the advection (e.g., Fig. 6 c). However, while the fine ($PM_{2.5F}$) to total (PM_{10T}) ratio for Si also increases (not shown in the figure), the ratio Ca_F/Ca_T remains constant. This is a confirming evidence of the understanding that the calcium (Feldspars in general)/aluminium-silicate ratio in observed mineral aerosols is higher in particles of larger sizes (e.g., silt, which is characterized by D > 2 μm) with respect to smaller ones (clays, which are characterized by D < 2 μm), e.g, Molinaroli et al. (1993); Claquin et al. (1999); Perlwitz et al. (2015). Furthermore, data in Fig. 6 also indicate wet removal as being more efficient on 5 μm sized particles than on 2 μm ones. Two processes may contribute to such effects: 1) the preferential nucleation of raindrops on soluble Ca-rich particles, followed by precipitation (e.g., Ohata et al., 2016), and 2) a preferential scavenging of aerosol particles larger than 2 μm in diameter. In this respect, Andronache (2003) demonstrates below-cloud scavenging by raindrops to be 2-3 orders of magnitude more effective on particles of diameters ranging between 3 and 10 μm, with respect to aerosol particles with diameters sized between 0.1 and 2 μm. Also considering that each nucleated rain-droplet contains hundreds of dust grains (e.g., Fig. A4.2), the selective wet-subsidence/removal mechanism appears to be the most likely driver of the observed depletion in the larger, Ca-rich particles. In fact, the strong precipitation affecting Plumes 2 and 3 on May 23 (9 UTC) selectively removed most of the particles larger than 5 μm. Conversely, 2 μm, 1 μm, and 0.56 μm sized particles remained unaffected. This condition persisted until the afternoon of May 24, when the dust plume extended back to ground level (e.g., Fig. 6). Such selective processes are also confirmed by the comparison of Saharan dust size distributions as collected in air versus those collected in rain water in Sardinia by Guerzoni et al. (1997). These authors reported wet-deposited dust to be richer in larger particles, to minimize in summer months, and to convey to the ground 2–2.5 times the mass associated with dry events. Section 3.2.2 shall further address size-resolved mineralogy of the dust collected during these advections.

It is worth mentioning that the SDA affected APS-measured particle concentrations down to aerodynamic diameters of about 0.8 μm, with minor modification of the smaller particles concentrations. The 0.8 μm dimensional class then represents the lower limit of the Saharan dust size distributions observed during the IOP.

Finally, the combined analysis of PLC and PIXE observations, together with BSC-DREAM8b, and WRF-Chem simulations confirms a good capability of the PLC depolarization signal at detecting SDA

layers. In particular, we find the 5% depolarization level as a good threshold to ascertain the presence of dust. The same analysis, also confirms good skills of the two models at determining the timing of the SDA. Conversely, the dust mass concentration estimates (PM_{10}) made by the two models are higher than those observed. (e.g., Section 3.1.2 and comparison of Figs. 6f and 8). One possible mechanism contributing to this discrepancy is the wet-removal process observed to act on the largest particles.

The following sections address some details about the chemical composition of the atmospheric aerosols as observed during the DIAPASON IOP2 by means of chemical analysis of 24-h PM_{10} filter (3.2.2, and Appendix C), PIXE analysis of hourly $PM_{2.5}$ and PM_{10} filters (Section 3.2.3, and Appendix B), and SEM mineralogy of 10-stage impactor filters (Section 3.2.4, and Appendix D).

3.2.2. PM chemical analysis

Aerosol chemical analysis has been performed on 24-h PM_{10} filters collected in the period 16–27 May, 2014, that is encompassing the peak of the Saharan dust advection event. Methods employed in the analysis are described in Appendix C. Fig. 7 illustrates the daily variation of PM_{10} macro-components resulting from this analysis. A remarkable increase in the concentration of soil-related components is observed during the days characterized by the dust intrusion. In particular, while before and after the SDA period the sum of soil-related elements is in the order of 5 μg/m³, it increases up to 22–23 μg/m³ at the peak of the event. In the periods before and after the advection, carbonates exceed silicates and organics exceed minerals. During the advection both ratios invert, silicates exceed carbonates and soil-related exceed total organic and inorganic aerosols. Furthermore, during the SDA the increase in soil-related elements is paralleled by an increase in PM-bound water. In this respect, previous studies have highlighted desert dust as being characterized by high water content (about 5% of the mass of soil-related components and up to 10% of the mass of PM_{10}), and that this specific water contribution is detected in the temperature range 100–180 °C when using the thermal-ramp Karl-Fisher method (Perrino et al., 2016). Moreover, the mass size distribution of PM-bound water during the study period has shown that in dust-affected days, when crustal species are the main PM components, water mass is distributed mainly in the coarse size range of silicates, and its size-distribution is very similar to that of desert dust chemical components (Canepari et al., 2017).
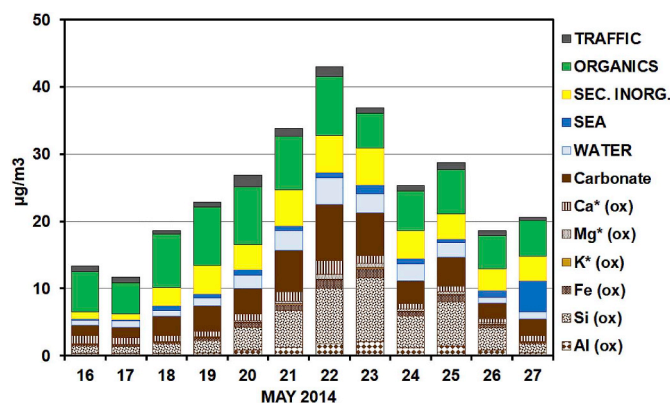

Fig. 7. Daily variation of PM_{10} macro-components (capital letters), and of PM-bound water as obtained from the chemical analysis of 24-h filters collected in the period 16–27 May, 2014. Soil components (in brown) are shown individually. The symbol * indicates the insoluble fraction, while (ox) indicates the use of correction factors for oxygen in metal oxides. (For interpretation of the references to colour in this figure legend, the reader is referred to the Web version of this article.)
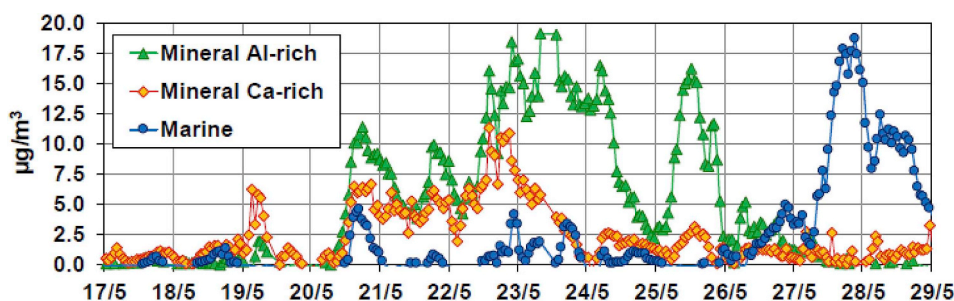
Fig. 8. Partitioning between the two mineral dust species associated with the SDA, and marine aerosol component as obtained by PMF analysis applied to PIXE data collected along with the DIAPASON IOP 2.

The time-variation of concentrations of individual soil-related components indicates that the loads of calcium and carbonate are the first to increase on May 18, then peaking on May 22, 2014. Conversely, concentrations of Al, Si and Fe increase only on May 20, then reaching a peak on May 23, 2014. This confirms the relative depletion in silt-rich versus clay-rich aerosol (e.g., Claquin et al., 1999) observed during the second part of the dust event, when the Si/Ca ratio and D ≤ 2 μm particles increase while D = 5 μm particles decrease (e.g. Section 3.2.1, Fig. 6d). This point will also be confirmed by the discussion of PIXE data in the following section.

3.2.3. PM bulk composition from PMF analysis of PIXE data

A source identification analysis combining the PIXE data of the whole PM_{10} load (e.g. Appendix B) and equivalent black carbon (eBC) data from MoLa (Drewnick et al., 2012) has been carried out by Positive Matrix Factorization (PMF) statistical analysis (Paatero and Hopke, 2003) using the US EPA PMF v5 software. Hourly-resolved PM_{10} mass concentration was derived from aerosol size distributions collected by the Aerodynamic Particle Sizer (APS, TSI, e.g., Appendix A), and used as "total variable" in PMF to obtain the absolute source profiles and weights. The APS-derived PM_{10} loads were checked to be in good agreement (mean differences of 10%) with PM_{10} high time resolution mass concentrations obtained by the MoLa Environmental Dust Monitor (Grimm EDM180, EU standard EN12341 compliant), which was only available past May 20, 2014 (Drewnick et al., 2012; Struckmeier et al., 2016). The Polissar et al. (1998) procedure was used to prepare the data and their associated uncertainties as the PMF input data. PMF solutions from 5 to 10 factors were systematically explored and the resulting Q values, the scaled residuals, and the F and G matrices were examined to find the best solution. The solution with seven factors (i.e., source types) was found to be the most realistic, the scaled residuals (i.e. the differences between measured and modelled, divided by the uncertainty) being almost normally distributed, and ranging between ± 3 for the majority of the species (more details given in Appendix B).

Four anthropogenic components/sources were identified: 1) a traffic-related source characterized by BC, Fe, Cu, associated with direct exhaust emission, abrasion of brakes and tires, and resuspension of the dust deposited on the roads, all showing the characteristic two-peak, rush-hour timing; 2) a sulphate-containing component, attributed to secondary sulphate and aged aerosols likely due to a regional background contribution; 3) A combustion-type source, characterized by high BC and K fingerprints; and 4) a component characterized by Zn and some Pb, possibly attributed to industrial emissions. In fact, some authors attributed these metals to emissions from smelters (e.g., Moreno et al., 2011; Amato et al., 2016), or to local workshops and ateliers (Richard et al., 2011). Some other authors found a similar source and attributed it to the combustion of municipal waste (Tan et al., 2002). Combustion and traffic-related sources, observed during IOP2, have been addressed in Struckmeier et al. (2016), and will not be discussed here.

Three natural components/sources were also identified by the PMF analysis: a sea-salt source primarily characterized by Na, Cl, S and Mg,

with inter-elemental ratios very close to those of the sea salt composition (Cl/Na = 1.8, Mg/Na = 0.13, S/Na = 0.08), plus two mineral dust sources characterized by high loadings of all soil-related elements (Si, Al, Mg, K, Ca, Ti, Mn, Fe) with enrichment factors very close to the ones typical of the earth crust (Mason, 1966). The main difference between the two mineral dust sources is the higher Ca enrichment factor (10 versus 1.5) of one with respect to the other. Both sources are clearly associated with the Saharan intrusion (that is, they are not of local origin) since they are only present during the transport event. The time evolution of the aerosol load associated with the three natural sources is shown in Fig. 8.

Together with the chemical analysis presented in the previous Section 3.2.2, these results tend to confirm the data interpretation formulated in Sections 2.2, and 3.2.1, that is, the Ca-rich mineral dust component being strongly depleted with respect to the Al-rich component after the intense wet removal events which occurred between 22 UTC of May 22, and 9UTC of May 23, 2014. Similar mechanisms possibly acted upon the Al-rich, precipitation-affected plume 4. The single particle's mineralogy addressed in the next section, will help detailing some features of the two different dust conditions.

Data in Fig. 6 also explain the noticeable decrease in depolarization observed starting May 26 (e.g., Fig. 6b) as an effect of the increasing marine (spherical) aerosols successively replacing the decreasing dust concentrations. The increase in the marine aerosol component is confirmed by the rising Cl concentrations in Fig. 6c.

3.2.4. PM mineralogy by SEM analysis

Mineralogy and composition assessment of the aerosol advected during IOP2 have been carried-out by SEM/XEDS analysis of filter-sampled dust. A single air sampling on a 10-stage impactor (e.g., Appendix D) was performed from 11am of May 21, through 11am of May 23, 2014, that is the period of highest concentrations of Ca-rich dust (e.g., 3.2.3). Some microphotographs of the sampled dust are presented in Appendix D.

Particles investigated by SEM/XEDS microanalysis were classified as: 1) Ca-rich carbonates and sulfates (Ca-rich); 2) silicates and silica (Si-rich); 3) Sodium-nitrate and Sodium-chloride (Na-rich); 4) K-rich phosphates mixed with other inorganic salts (Salts), and 5) carbonaceous particles (C-rich). In fact, the share of the latter class (C-rich) was found to be negligible, therefore it is not considered in the following discussion. The Ca-rich (1), Na-rich (3) and salts (4) classes are mainly composed of Calcium-carbonate, Sodium-nitrate and Potassium-phosphate, respectively. These species should be thus considered as the markers for the above mentioned particulate components. Due to the contribution of the aluminum foils used as collection support in the cascade impactor, further discrimination into silicates and silica was not possible for the Si-rich (2) class. For the goals of this analysis, only the Ca-rich (1), and Si-rich (2) particles will be discussed hereafter.

Fig. 9 reports the overall number and volume size distributions of the Ca-rich (1) and Si-rich (2) particles collected along the 48 h in the four-bin size range 1–10 μm. The four central bin sizes are 1.4, 2.5, 4.4, and 7.8 μm, respectively. In both distributions, the Si-rich fraction is
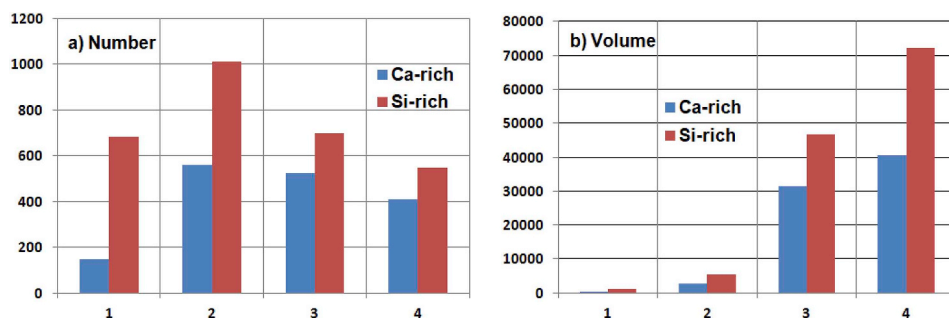
Fig. 9. Number (a) and volume (b) distributions of the Ca-rich (blue bars) and Si-rich (red bars) particles, as obtained by SEM/XEDS analysis of the range 1–10 μm of multi-stage impactor filters collected in the time-span May 21-May 23, 2014 (DIAPASON's IOP2). The central bin sizes of the four stages (1–4) are 1.4, 2.5, 4.4, and 7.8 μm, respectively. (For interpretation of the references to colour in this figure legend, the reader is referred to the Web version of this article.)

always found to be larger than the Ca-rich one. At the same time, the ratio Si-rich/Ca-rich decreases with increasing size for both number and volume distributions. In the case of volume distribution, this ratio is 2.9, 2, 1.5, and 1.8, respectively. The larger Si-rich/Ca-rich ratios observed at smaller sizes are in good agreement with the elevated values of the Si/Ca ratio found in the period May 23–25, when both Calcium (from PIXE), and particles with sizes larger than 2 μm (from APS), were strongly depleted in the dust plume, possibly by precipitation events (see discussion related to Fig. 6). In the same way, a decrease in the Si/Ca ratio and a sharp increase in 5 μm particles concentrations, as observed on May 19 during light, evaporating precipitation events, appear to be well explained by the preferential subsidence of particle of larger sizes caused by warm rain. Overall, this analysis supports the previous interpretation of a preferential wet removal of coarser particles (> 2 μm) and of a larger relative abundance of Ca-rich (with respect to Si-rich) aerosol particles in this coarser fraction.

3.2.5. Time-resolved PM_1 composition

Starting on the afternoon of May 20, PM concentrations and PM_1 chemical composition were measured using the Mobile Laboratory MoLa (Drewnick et al., 2012; Struckmeier et al., 2016) at the ISAC Rome Tor Vergata site. In Fig. 10, highly time-resolved data (5-min data, panel a) as well as daily averages (panel b) of fine (PM_1) and coarse ($PM_{10-2.5}$) particle concentrations as well as PM_1 chemical composition are shown. Aerosol composition was measured by HR-ToF AMS (Aerodyne Res. Inc.: sulphate, nitrate, ammonium, organics) and a black carbon monitor (MAAP, Thermo Sci. Inc.: equivalent BC).

In good agreement with the PLC observations presented in Section 3.2.1, and Fig. 6, coarse particle concentrations peak on the afternoon and night of May 22 (Fig. 10a), when plume 2 descends down to ground

level and show a secondary peak on May 25, when plume 4 (Section 3.2.1) reaches the ground. Already on May 20, elevated coarse particle concentrations, with respect to post-SDA event concentrations (after May 27), were observed. This agrees well with the timing of ground contact of plume 1 as discussed in Section 3.2.

Contrary to the coarse particle concentrations, which peak on May 22 and then strongly decrease until May 27, daily averaged PM_1 concentrations start at an elevated level at the beginning of the measurements and decrease only slightly throughout the SDA event (Fig. 10b) before they drop to background values on May 27. The highly time-resolved data (panel a) do not show a strong correlation of PM_1 concentrations with those of the coarse particles, reflecting the different sources which were dominating the two aerosol modes. For PM_1 sulphate, nitrate and ammonium, no general trend over the SDA event and no strong daily variations were found. These aerosol components are mainly associated with aged secondary aerosols and therefore only slightly affected by local source or mixing layer height dynamics. On the other hand, PM_1 organics and equivalent black carbon show the decreasing trend over the SDA event (panel b), but also strong diurnal variability according to emission dynamics of local sources like traffic or cooking activities, with peak concentrations during rush-hour and meal times (panel a, Struckmeier et al., 2016).

Even though no data were available from before the event, due to the beginning of the MoLa measurements just before the peak of the SDA, these results suggest that PM_1 is not directly affected in a significant way by the dust intrusion, but indirectly by meteorological conditions associated with the onset of the SDA, as low TKE and high atmospheric pressure (e.g., Figs. 4 and 5). These conditions support the accumulation of aerosol, related to local emission sources like traffic or cooking activities, while advected secondary aerosols are less affected.
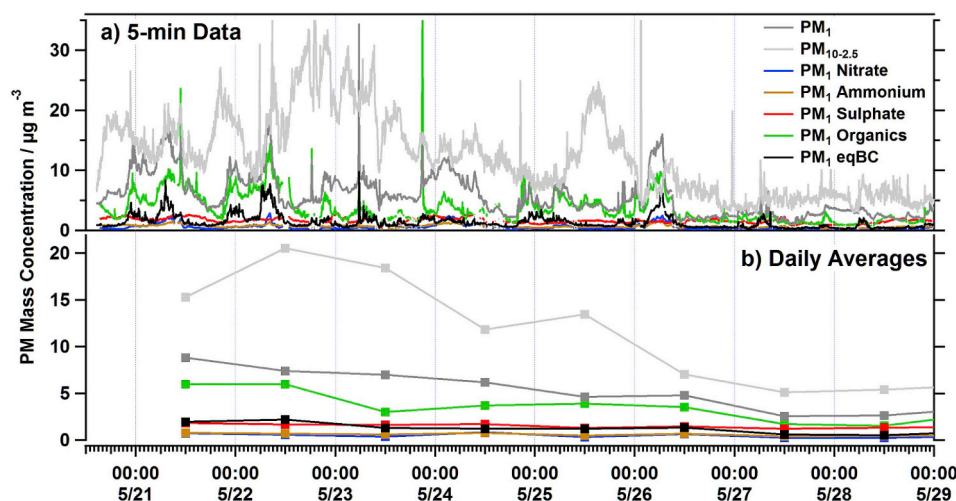

Fig. 10. Temporal evolution of fine (PM_1) and coarse ($PM_{10-2.5}$) particle concentrations as well as AMS PM_1 chemical composition for the SDA event observed during IOP2 at the ISAC Rome Tor Vergata site, presented as high time-resolution data (panel a) and daily averaged concentrations (panel b).

4. Main outcomes and conclusions

Analysis of observations and model simulations carried-out along the LIFE + DIAPASON project (2011–2015) provided new insight into the processes generating and governing the advection and deposition of Saharan dust to the southern Europe, central Mediterranean region. Physical and chemical properties of the dust advected to Rome (Italy) have been characterized in depth, using, amongst others, new techniques as the polarization lidar-ceilometer (PLC) one.

In the period October 2011–September 2014, Saharan dust advections were found to occur over Rome on about 32% of the days. Some 30% of the advection's time involved wet deposition, while 70% was associated with dry deposition. This latter number matches the frequency of SDA dry deposition events observed at ground in Rome in the period 2001–2004 (Gobbi et al., 2013). While 33% of the total dry deposition events occurred in summer, only 11% of wet deposition events occurred in that season. The Grand Erg Oriental at 33N (southern slopes of the Atlas range, between Algeria and Tunisia) was confirmed as the most frequent region of origin of the dust mobilized towards central Italy. Secondary source regions include northern Morocco and Libya. Saharan advections in Rome were usually preceded by increasing atmospheric pressure and decreasing TKE. These conditions favour the accumulation of aerosols associated to local emission sources before the actual arrival to the ground of the SDA. In fact, both PM_1 (BC and organics during IOP2), and PM_{10} were observed to increase before the dust plume reached the ground. A pressure drop, frequently accompanied by rainfall, then characterized the dust event period. In general, meteorology (precipitation and turbulence *in primis*) resulted to be an important modulator of PM loads. These results indicate that together with the exact timing of the events, meteorology should always be considered in the analysis of both the dust share in PM_{10} loads, and of the health effects of SDA events.

Detailed analysis of an SDA during the DIAPASON May 2014 IOP showed the advection to affect particle concentrations down to diameters of about 0.8 μm. In the range 1–10 μm, number size distributions of the advected dust peaked in the 2.5 μm diameter range. Conversely, volume size distributions peaked at the largest sizes, were the Ca-rich component becomes relatively more important. Rainfall was observed to preferentially remove particles larger than 2 μm, thus causing a significant depletion in the dust, Ca-rich fraction with respect to the Si-rich one. Wet-removal processes appear then to be rather effective at changing the composition and size distribution of the Saharan dust before it reaches the ground.

The combined analysis of PLC, standard chemistry, and PIXE observations, together with DREAM8b, and WRF-Chem numerical simulations confirmed the good capability of the PLC depolarization signal at detecting SDA layers. We found exceedance of the 5% depolarization level to be a good threshold to indicate the presence of dust.

Model forecasts demonstrated to perform rather well at predicting the timing of SDA evolution, not so well at predicting dust loads. Combination of methodologies (modelling and PLC observations) was found to be an effective way to predict and 'certify' the presence of Saharan dust on the basis of 'online' information. Conversely, both PIXE, chemical and mineralogical analysis provided (off-line) reliable evidence of the presence of Saharan dust. In general, this presence was associated with a significant increase in Si-rich particles. A non-negligible fraction of water was also observed to be associated with the Si-rich component of dust. The hourly PIXE records of the Si/Ca ratio increasing above 1 were found to represent a robust marker of the presence and evolution of the Saharan dust loads.

Dry deposition of Saharan dust was observed to occur in Rome on about 22% of the time, bringing in these days an average PM_{10} increase of the order of 10 μg/m^3. These results are consistent with the findings and extend the statistics on SDA properties we set off over a decade ago (Gobbi et al., 2013).

Appendix A. Supplementary data

Supplementary data to this article can be found online at https://doi.org/10.1016/j.atmosenv.2019.01.002.

References

Alpert, P., Krichak, S.O., Tsidulko, M., Shafir, H., Joseph, J.H., 2002. A dust prediction system with TOMS initialization. Mon. Weather Rev. 130, 2335–2345.

Amato, F., Alastuey, A., Karanasiou, A., Lucarelli, F., Nava, S., Calzolai, G., Severi, M., Becagli, S., Gianelle, V.L., Colombi, C., Alves, C., Custodio, D., Nunes, T., Cerqueira, M., Pio, C., Eleftheriadis, K., Diapouli, E., Reche, C., Minguillon, M.C., Manousakas, M.-I., Maggos, T., Vratolis, S., Harrison, R.M., Querol, X: AIRUSE-LIFE +: A harmonized PM speciation and source apportionment in five southern European cities. Atmos. Chem. Phys. 16, 3289e3309. https://doi.org/10.5194/acp-16-3289-2016.

Andronache, C., 2003. Estimated variability of below-cloud aerosol removal by rainfall for observed aerosol size distributions. Atmos. Chem. Phys. 3, 131–143.

Angelini, F., Gobbi, G.P., 2014. Some remarks about lidar data pre-processing and different implementations of the gradient method for determining the aerosol layers. Ann. Geophys. 57 (2), A0218. https://doi.org/10.4401/ag-6408.

Ansmann, A., Bösenberg, J., Chaikovsky, A.P., Comerón, A., Eixmann, R., Freudenthaler, V., Ginoux, P., Konguem, L., Linné, H., Márquez, M.Á.L., Manoj, S., Matthias, V., Mattis, I., Mitev, V., Müller, D., Nickovic, S., Pelon, J., Sauvage, L., Sobolewsky, P., Stohl, A., Torres, O., Vaughan, G., Wandinger, U., Wiegner, M., 2003. Long-range transport of Saharan dust to northern Europe: the 11-16 October 2001 outbreak with EARLINET. J. Geophys. Res. 108, 4783. https://doi.org/10.1029/2003JD003757.

Antoine, D., Nobileau, D., 2006. Recent increase of Saharan dust transport over the Mediterranean Sea, as revealed from ocean color satellite (SeaWiFS) observations. J. Geophys. Res. 111, D12214. https://doi.org/10.1029/2005JD006795.

Ashpole, I., Washington, R., 2012. An automated dust detection using SEVIRI: a multiyear climatology of summertime dustiness in the central and Western Sahara. J. Geophys. Res. 117, D08202. https://doi.org/10.1029/2011JD016845.

Barnaba, F., Gobbi, G.P., 2004. Aerosol seasonal variability over the Mediterranean region and relative impact of maritime, continental and Saharan dust particles over the basin from MODIS data in the year 2001. Atmos. Chem. Phys. 4, 2367–2391.

Barnaba, F., Bolignano, A., Di Liberto, L., Morelli, M., Lucarelli, F., Nava, S., Perrino, C., Canepari, S., Basart, S., Costabile, F., Dionisi, D., Ciampichetti, S., Sozzi, R., Gobbi, G.P., 2017. desert dust contribution to PM_{10} loads in Italy: methods and recommendations addressing the relevant european commission Guidelines in support to the air quality directive 2008/50. Atmos. Environ. 161, 288–305. https://doi.org/10.1016/j.atmosenv.2017.04.038.

Basart, S., Pérez, C., Nickovic, S., Cuevas, E., Baldasano, J.M., 2012. Development and evaluation of the BSC-DREAM8b dust regional model over Northern Africa, the Mediterranean and the Middle East. Tellus B: Chem. Phys. Meteorol. 64 (1), 18539. https://doi.org/10.3402/tellusb.v64i0.18539.

Bréon, F.M., Vermeulen, A., Descloitres, J., 2011. An evaluation of satellite aerosol products against sunphotometer measurements. Remote Sens. Environ. 115, 3102–3111.

Calzolai, G., Lucarelli, F., Chiari, M., Nava, S., Giannoni, M., Carraresi, L., Prati, P., Vecchi, R., 2015. Improvements in PIXE analysis of hourly particulate matter samples. Nucl. Instrum. Methods B 363, 99e104.

Canepari, S., Simonetti, G., Perrino, C., 2017. Mass size distribution of particle-bound water. Atmos. Environ. 165, 45–56.

Claquin, T., Schulz, M., Balkanski, Y.J., 1999. Modelling the mineralogy of atmospheric dust sources. J. Geophys. Res. 104 (D18), 22243–22256.

Dewitte, O., Jones, A., Spaargaren, O., Breuning-Madsen, H., Brossard, M., Dampha, A., Deckers, J., Gallali, T., Hallett, S., Jones, R., Kilasara, M., Le Roux, P., Michaeli, E., Montanarella, L., Thiombiano, L., Van Ranst, E., Yemefack, M., Zougmore, R., 2013. Harmonisation of the soil map of Africa at the continental scale. Geoderma 211–212, 138–153.

Diémoz, H., Barnaba, F., Magri, T., Pession, G., Dionisi, D., Pittavino, S., Tombolato, I.K.F., Campanelli, M., Della Ceca, L.S., Hervo, M., Di Liberto, L., Ferrero, L., Gobbi,

G.P., 2018. Transport of Po Valley aerosol pollution to the northwestern Alps. Part 1: phenomenology. Atmos. Chem. Phys. Discuss in review. https://doi.org/10.5194/acp-2018-960.

Dionisi, D., Barnaba, F., Diémoz, H., Di Liberto, L., Gobbi, G.P., 2018. A multi-wavelength numerical model in support of quantitative retrievals of aerosol properties from automated lidar ceilometers and test applications for AOT and PM10 estimation. Atmos. Meas. Tech. 11, 6013–6042. https://doi.org/10.5194/amt-11-6013-2018.

Drewnick, F., Böttger, T., von der Weiden-Reinmüller, S.-L., Zorn, S.R., Klimach, T., Schneider, J., Borrmann, S., 2012. Design of a mobile aerosol research laboratory and data processing tools for effective stationary and mobile field measurements. Atmos. Meas. Tech. 5, 1443–1457. https://doi.org/10.5194/amt-5-1443-2012.

EC-2011, 2011. Establishing Guidelines for Demonstration and Subtraction of Exceedances Attributable to Natural Sources under the Directive 2008/50/EC on Ambient Air Quality and Cleaner Air for Europe. pp. 38. February, 2011. available at: http://register.consilium.europa.eu/doc/srv?l¼EN%25f¼4ST%206771%202011%20INIT.

Eresmaa, N., Karppinen, A., Joffre, S.M., Räsänen, J., Talvitie, H., 2006. Mixing height determination by ceilometer. Atmos. Chem. Phys. 6, 1485–1493. https://doi.org/10.5194/acp-6-1485-2006.

Evan, A.T., Flamant, C., Gaetani, M., Guichard, F., 2016. The past, present and future of African dust. Nature 31, 493–495. https://doi.org/10.1038/nature17149.

Fiedler, S., Schepanski, K., Knippertz, P., Heinold, B., Tegen, I., 2014. How important are atmospheric depressions and mobile cyclones for emitting mineral dust aerosol in North Africa? Atmos. Chem. Phys. 14, 8983–9000. https://doi.org/10.5194/acp-14-8983-2014.

Fiedler, S., Kaplan, M.L., Knippertz, P., 2015. The importance of Harmattan surges for the emission of North African dust aerosol. Geophys. Res. Lett. 42, 9495–9504. https://doi.org/10.1002/2015GL065925.

Garratt, J.R., 1994. The atmospheric boundary layer. Earth Sci. Rev. 37, 89–134.

Gaetani, M., Pasqui, M., Crisci, A., Guarnieri, F., 2012. A synoptic characterization of the dust transport and associated thermal anomalies in the Mediterranean basin. Int. J. Climatol. 36, 2779–2791. https://doi.org/10.1002/joc.3615.

Georgoulias, A.K., Tsikerdekis, A., Amiridis, V., Marinou, E., Benedetti, A., Zanis, P., Alexandri, G., Mona, L., Kourtidis, K.A., Lelieveld, J., 2018. A 3-D evaluation of the MACC reanalysis dust product over Europe, northern Africa and Middle East using CALIOP/CALIPSO dust satellite observations. Atmos. Chem. Phys. 18, 8601–8620. https://doi.org/10.5194/acp-18-8601-2018.

Ginoux, P., Prospero, J.M., Gill, T.E., Hsu, N.C., Zhao, M., 2012. Global-scale attribution of anthropogenic and natural dust sources and their emission rates based on MODIS Deep Blue aerosol products. Rev. Geophys. 50, RG3005. https://doi.org/10.1029/2012RG000388.

Gkikas, A., Houssos, E.E., Hatzianastassiou, N., Papadimas, C.D., Bartzokas, A., 2012. Synoptic conditions favouring the occurrence of aerosol episodes over the broader Mediterranean basin. Q. J. R. Meteorol. Soc. 138, 932–949. https://doi.org/10.1002/qj.978.

Gkikas, A., Hatzianastassiou, N., Mihalopoulos, N., Katsoulis, V., Kazadzis, S., Pey, J., Querol, X., Torres, O., 2013. The regime of intense desert dust episodes in the Mediterranean based on contemporary satellite observations and ground measurements. Atmos. Chem. Phys. 13, 12135e–12154e. https://doi.org/10.5194/acp-13-12135-2013.

Gkikas, A., Basart, S., Hatzianastassiou, N., Marinou, E., Amiridis, V., Kazadzis, S., Pey, J., Querol, X., Jorba, O., Gassó, S., Baldasano, J.M., 2016. Mediterranean intense desert dust outbreaks and their vertical structure based on remote sensing data. Atmos. Chem. Phys. 16, 8609–8642. https://doi.org/10.5194/acp-16-8609-2016.

Gobbi, G.P., 1998. Polarization lidar returns from aerosols and thin clouds: a framework for the analysis. Appl. Opt. 37, 5505–5508.

Gobbi, G.P., Barnaba, F., Giorgi, R., Santacasa, A., 2000. Altitude-resolved properties of a Saharan dust event over the Mediterranean. Atmos. Environ. 34, 5119–5127.

Gobbi, G.P., Barnaba, F., Van Dingenen, R., Putaud, J.P., Mircea, M., Facchini, M.C., 2003. Lidar and in situ observations of continental and Saharan aerosol: closure analysis of particles optical and physical properties. Atmos. Chem. Phys. 3, 2161–2172.

Gobbi, G.P., Barnaba, F., Ammannato, L., 2004. The vertical distribution of aerosols, Saharan dust and cirrus clouds in Rome (Italy) in the year 2001. Atmos. Chem. Phys. 4, 351–359.

Gobbi, G.P., Barnaba, F., Ammannato, L., 2007. Estimating the impact of Saharan dust on the year 2001 PM₁₀ record of Rome, Italy. Atmos. Env. 41, 261–275.

Gobbi, G.P., Angelini, F., Barnaba, F., Costabile, F., Baldasano, J.M., Basart, S., Sozzi, R., Bolignano, A., 2013. Changes in particulate matter physical properties during Saharan advections over Rome (Italy): a four-year study, 2001–2004. Atmos. Chem. Phys. 13, 7395–7404. https://doi.org/10.5194/acp-13-7395-2013.

Goudie, A.S., Middleton, N.J., 2001. Saharan dust storms: nature and consequences. Earth Sci. Rev. 56, 179–204.

Grell, G.A., Peckham, S.E., Schmitz, R., McKeen, S.A., Frost, G., Skamarock, W.C., Eder, B., 2005. Fully coupled 'online' chemistry within the WRF model. Atmos. Environ. 39, 6957–6976.

Guerzoni, S., Molinaroli, E., Chester, R., 1997. Saharan dust inputs to the western Mediterranean Sea: depositional patterns, geochemistry and sedimentological implications. Deep-Sea Res. II 44 (34), 630.

Haeffelin, M., Angelini, F., Morille, Y., Martucci, G., Frey, S., Gobbi, G.P., Lolli, S., O'Dowd, C.D., Sauvage, L., Xueref-Rémy, I., Wastine, B., Feist, D.G., 2011. Evaluation of mixing-height retrievals from automatic profiling lidars and ceilometers in view of future integrated networks in Europe. Boundary-Layer Met. https://doi.org/10.1007/s10546-011-9643-z.

Journet, E., Balkanski, Y., Harrison, S.P., 2014. A new data set of soil mineralogy for dust-cycle modeling. Atmos. Chem. Phys. 14, 3801–3816. https://doi.org/10.5194/acp-14-3801-2014. 2014.

Kallos, G., Nickovic, S., Papadopoulos, A., Jovic, D., Kakaliagou, O., Misirlis, N., Boukas, L., Mimikou, N., Sakellaridis, G., Papageorgiou, J., Anadranistakis, E., Manousakis, M., 15–17 Oct., 1997. The Regional Weather Forecasting System SKIRON: an Overview Paper Presented at the International Symposium on Regional Weather Prediction on Parallel Computer Environments. University of Athens, Athens, Greece.

Kallos, G., Astitha, M., Katsafados, P., Spyrou, C., 2007. Long-range transport of anthropogenically and naturally produced particulate matter in the Mediterranean and North Atlantic: current state of knowledge. J. Appl. Meteorol. Clim. 46, 1230–1251.

Kaufman, Y.J., Tanré, D., Boucher, O., 2002. A satellite view of aerosols in the climate system. Nature 419, 215–223.

Kishcha, P., Alpert, P., Shtivelman, A., Krichak, S.O., Joseph, J.H., Kallos, G., Katsafados, P., Spyrou, C., Gobbi, G.P., Barnaba, F., Nickovic, S., Perez, C., Baldasano, J.M., 2007. Forecast errors in dust vertical distributions over Rome (Italy): multiple particle size representation and cloud contributions. J. Geophys. Res. 112, D15205. https://doi.org/10.1029/2006JD007427.

Knippertz, P., Todd, M.C., 2012. Mineral dust aerosols over the Sahara: meteorological controls on emission and transport and implications for modeling. Rev. Geophys. 50, RG1007. https://doi.org/10.1029/2011RG000362.

Knippertz, P.,J., Stuut, B.W., 2014. Mineral Dust: A Key Player in the Earth System. Springer, Dordrecht, pp. 509.

Liu, Z., Vaughan, M., Winker, D., Kittaka, C., Getzewich, B., Kuehn, R., Hostetler, C., 2009. The CALIPSO lidar cloud and aerosol discrimination: version 2 algorithm and initial assessment of performance. J. Atmos. Ocean. Tec. 26 (7), 1198–1213.

Lucarelli, F., Calzolai, G., Chiari, M., Giannoni, M., Mochi, D., Nava, S., Carraresi, L., 2014. The upgraded external-beam PIXE/PIGE set-up at LABEC for very fast measurements on aerosol samples. Nucl. Instrum. Methods B 318, 55–64.

Lucarelli, F., Calzolai, G., Chiari, M., Nava, S., Carraresi, L., 2018. Study of atmospheric aerosols by IBA techniques: the LABEC experience. Nucl. Instrum. Methods B 417, 121–127.

Mallone, S., Stafoggia, M., Faustini, A., Gobbi, G.P., Marconi, A., Forastiere, F., 2011. Saharan dust and associations between particulate matter and daily mortality in Rome, Italy. Env. Health Persp. 119 (10), 1409–1414. https://doi.org/10.12989/ehp.1003026.

Mason, B., 1966. Principles of Geochemistry, third ed. Wiley, New York.

McGill, M.J., Hlavka, D.L., Hart, W.D., Spinhirne, J.D., Scott, V.S., Schmid, B., 2002. The cloud physics lidar: instrument description and initial measurement results. Appl. Opt. 41, 3725–3734.

Molinaroli, E., Guerzoni, S., Rampazzo, G., 1993. Contribution of Saharan dust to the central Mediterranean basin, Processes controlling the composition of clastic sediments. In: Johnsson, M.J., Basu, A. (Eds.), Boulder CO, Geological Society of America Special Paper. vol. 284. pp. 303–312.

Moreno, T., Querol, X., Alastuey, A., Reche, C., Cusack, M., Amato, F., Pandolfi, M., Pey, J., Richard, A., Prevot, A.S.H., Furger, M., Gibbons, W., 2011. Variations in time and space of trace metal aerosol concentrations in urban areas and their surroundings. Atmos. Chem. Phys. 11, 9415–9430. https://doi.org/10.5194/acp-11-9415-2011.

Nava, S., Becagli, S., Calzolai, G., Chiari, M., Lucarelli, F., Prati, P., Traversi, R., Udisti, R., Valli, G., Vecchi, R., 2012. Saharan dust impact in central Italy: an overview on three-year elemental data records. Atmos. Environ. 60, 444–452.

Ohata, S., Moteki, N., Mori, T., Koike, M., Kondo, Y., 2016. A key process controlling the wet removal of aerosols: new observational evidence. Sci. Rep. 6 (34113). https://doi.org/10.1038/srep34113.

Paatero, P., Hopke, P.K., 2003. Discarding or down-weighting high noise variables in factor analytic models. Anal. Chim. Acta 490, 277–289.

Pandolfi, M., Tobias, A., Alastuey, A., Sunyer, J., Schwartz, J., Lorente, J., Pey, J., Querol, X., 2014. Effect of atmospheric mixing layer depth variations on urban air quality and daily mortality during Saharan dust outbreaks. Sci. Total Environ. 494–495, 283–289. https://doi.org/10.1016/j.scitotenv.2014.07.0042014.

Papayannis, A., Amiridis, V., Mona, L., Tsaknakis, G., Balis, D., Bösenberg, J., Chaikovski, A., De Tomasi, F., Grigorov, I., Mattis, I., Mitev, V., Müller, D., Nickovic, S., Pérez, C., Pietruczuk, A., Pisani, G., Ravetta, F., Rizi, V., Sicard, M., Trickl, T., Wiegner, M., Gerding, M., Mamouri, R.E., D'Amico, G., Pappalardo, G., 2008. Systematic lidar observations of Saharan dust over Europe in the frame of EARLINET (2000-2002)". J. Geophys. Res. 113. https://doi.org/10.1029/2007JD009028.

Perez, L., Tobias, A., Querol, X., Kunzli, N., Pey, J., Alastuey, A., Viana, M., Valero, N., Gonzalez-Cabre´, M., Sunyera, J., 2008. Coarse particles from Saharan dust and daily mortality. Epidemiology 19 (6).

Perlwitz, J.P., Pérez García-Pando, C., Miller, R.L., 2015. Predicting the mineral composition of dust aerosols – Part 2: model evaluation and identification of key processes with observations. Atmos. Chem. Phys. 15, 11629–11652. https://doi.org/10.5194/acp-15-11629-2015.

Perrino, C., Catrambone, M., Farao, C., Canepari, S., 2016. Assessing the contribution of water to the mass closure of PM₁₀. Atmos. Environ. 140, 555–564.

Pey, J., Querol, X., Alastuey, A., Forastiere, F., Stafoggia, M., 2013. African dust outbreaks over the Mediterranean Basin during 2001–2011: PM₁₀ concentrations, phenomenology and trends, and its relation with synoptic and mesoscale meteorology. Atmos. Chem. Phys. 13, 1395–1410. https://doi.org/10.5194/acp-13-1395-2013.

Pietrodangelo, A., Salzano, R., Bassani, C., Pareti, S., Perrino, C., 2015. Composition, size distribution, optical properties, and radiative effects of laboratory-resuspended PM₁₀ from geological dust of the Rome area, by electron microscopy and radiative transfer modelling. Atmos. Chem. Phys. 15, 13177–13194. https://doi.org/10.5194/acp-15-13177-2015.

Polissar, A.V., Hopke, P.K., Paatero, P., 1998. Atmospheric aerosol over Alaska: 2. Elemental composition and sources. J. Geophys. Res. 19045–19057.

Prospero, J.M., Ginoux, P., Torres, O., Nicholson, S.E., Gill, T.E., 2002. Eenvironmental characterization of global sources of atmospheric soil dust identified with the nimbus 7 total ozone mapping spectrometer (TOMS) absorbing aerosol product. Rev. Geophys. 40 (1).

Querol, X., Pey, J., Pandolfi, M., Alastuey, A., Cusack, M., Perez, N., Moreno, T., Viana, M., Mihalopoulos, N., Kallos, G., Kleanthous, S., 2009. African dust contributions to mean ambient PM₁₀ mass-levels across the Mediterranean Basin. Atmos. Environ. 43 (28), 4266–4277.

Richard, A., Gianini, M.F.D., Mohr, C., Furger, M., Bukowiecki, N., Minguill´on, M.C., Lienemann, P., Flechsig, U., Appel, K., De Carlo, P.F., Heringa, M.F., Chirico, R.,

Baltensperger, U., Prevot, A.S.H., 2011. Source apportionment of size and time resolved trace elements and organic aerosols from an urban courtyard site in Switzerland. Atmos. Chem. Phys. 11, 8945–8963. https://doi.org/10.5194/acp-11-8945-2011.

Rizza, U., Barnaba, F., Miglietta, m., Mangia, C., Di Liberto, L., Dionisi, D., Costabile, F., Grasso, F., Gobbi, G.P., 2017. WRF-Chem model simulations of a dust outbreak over the central Mediterranean and comparison with multi-sensor desert dust observations. Atmos. Chem. Phys. 17 (1), 93–115.

Sakai, T., Nagai, T., Zaizen, Y., Mano, Y., 2010. Backscattering linear depolarization ratio measurements of mineral, sea-salt, and ammonium sulfate particles simulated in a laboratory chamber. Appl. Opt. 49, 4441. https://doi.org/10.1364/AO.49.004441.

Sassen, K., 1991. The polarization lidar technique for cloud research: a review and current assessment. Bull. Am. Met. Soc. 71, 1848–1866.

Seibert, P., Beyrich, F., Gryning, S.E., Joffre, S., Rasmussen, A., Tercier, P., 2000. Review and intercomparison of operational methods for the determination of the mixing height. Atmos. Environ. 34, 1001–1027. https://doi.org/10.1016/S1352-2310(99)00349-0.

Srivastava, M.K., Sarthi, P.P., 2002. Turbulent kinetic energy in the atmospheric surface layer during the summer monsoon. Met. Applic. 9, 239–246.

Stafoggia, M., Zauli-Sajani, S., Pey, J., Samoli, E., Alessandrini, E., Basagaña, X., Cernigliaro, A., Chiusolo, M., Demaria, M., Díaz, J., Faustini, A., Katsouyanni, K., Kelessis, A.G., Linares, C., Marchesi, S., Medina, S., Pandolfi, P., Pérez, N., Querol, X., Randi, G., Ranzi, A., Tobias, A., Forastiere, F., 2016. MED-PARTICLES Study Group.

Desert dust outbreaks in Southern Europe: contribution to daily PM10 concentrations and short-term associations with mortality and hospital admissions. Environ. Health Perspect. 124, 413–419. https://doi.org/10.1289/ehp.1409164.

Stein, A.F., Draxler, R.R., Rolph, G.D., Stunder, B.J.B., Cohen, M.D., Ngan, F., 2015. NOAA's HYSPLIT atmospheric transport and dispersion modeling system. Bull. Amer. Meteor. Soc. 96, 2059–2077. https://doi.org/10.1175/BAMS-D-14-00110.1.

Struckmeier, C., Drewnick, F., Fachinger, F., Gobbi, G.P., Borrmann, S., 2016. Atmospheric aerosols in Rome, Italy: sources, dynamics and spatial variations during two seasons. Atmos. Chem. Phys. 16, 15277–15299. https://doi.org/10.5194/acp-16-15277-2016.

Tafuro, A.M., Barnaba, F., De Tomasi, F., Perrone, m.r., Gobbi, G.P., 2006. Saharan dust particle properties over the central Mediterranean. Atmos. Res. 81 (1), 67–93.

Tan, P.V., Fila, M.S., Evans, G.J., Jervis, R.E., 2002. Aerosol laser ablation mass spectrometry of suspended powders from PM sources and its implications to receptor modelling. J. Air Waste Manag. 52, 27–40.

Weitkamp, C. (Ed.), 2005. LIDAR: Range-Resolved Optical Remote Sensing of the Atmosphere. Springer series in optical sciences, pp. 455 ISSN 0342-4111, 102.

Wiegner, M., Geiß, A., 2012. Aerosol profiling with the Jenoptik ceilometer CHM15kx. Atmos. Meas. Techn. 5 (8) 1953.

Winker, D.M., Vaughan, M.A., Omar, A., Hu, Y., Powell, K.A., Liu, Z., Young, S.A., 2009. Overview of the CALIPSO mission and CALIOP data processing algorithms. J. Atmos. Ocean. Technol. 26 (11), 2310–2323.